Carbon Support Corrosion in PEMFCs Followed by Identical Location Electron Microscopy

ACS Catalysis

pubs.acs.org/acscatalysis
Research Article

Carbon Support Corrosion in PEMFCs Followed by Identical Location Electron Microscopy

Linnéa Strandberg,*[,‖] Victor Shokhen,[‖] Magnus Skoglundh, and Björn Wickman*

Cite This: ACS Catal. 2024, 14, 8494−8504

ABSTRACT: Identical location scanning electron microscopy (IL-SEM) and transmission electron microscopy (IL-TEM) are used to follow the degradation of the cathodic catalytic Pt/C electrode layer in a real proton-exchange membrane fuel cell under operation. During an accelerated stress test, mimicking start-up/shutdown conditions, the IL-SEM analysis reveals the formation and growth of cracks in the electrode layer, which expose the underlying membrane, leading to the creation of isolated islands of the electrode layer that tend to delaminate from the membrane. This is found to correlate with a 2- to 4-fold increase of the cell resistance. Nanoscale IL-TEM imaging shows that the diameter of the primary particles of the carbon support shrinks by on average 20%. Consequently, the Pt particles on the support agglomerate and grow by 63% contributing to an observed 65% loss in the electrochemically active surface area. The corrosion of the structural weak points of the carbon support leads to structural collapse. This collapse of the porous structure and weakening of connective points within the cathodic catalyst layers coincide with increased cell and mass transport resistance, resulting in large performance losses. While similar effects have been indicated before, the IL microscopy analysis provides a deeper understanding of the underlying mechanisms and the connection between morphological changes and fuel cell performance losses.

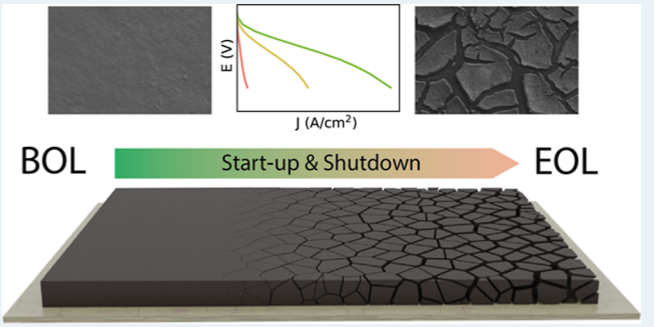

KEYWORDS: *PEMFC, platinum degradation, carbon corrosion, identical location TEM, identical location SEM*

1. INTRODUCTION

Proton-exchange membrane fuel cells (PEMFCs) have emerged as a promising technology for clean energy conversion, with the potential for zero emissions of greenhouse gases and high efficiency, making PEMFCs a viable alternative to traditional fossil fuel-based systems used for transport and stationary power generation.[1−3] However, despite their potential, several challenges limit the widespread adoption of PEMFCs, including the high cost of Pt used in the catalysts and degradation issues caused by the harsh and varying operational conditions that PEMFCs endure.[2,4] Degradation of the catalyst layers (CLs), in particular, can lead to a considerable decrease in the performance. A better understanding of the degradation mechanisms is fundamental in the development of new materials with improved stability or to optimize the control of the fuel cell to avoid the most degrading conditions and, thus, achieve a longer lifetime.

Degradation of the CLs is a complex process that is heavily affected by the operational conditions of the fuel cell, such as varying voltage, relative humidity, and temperature. Under normal operating conditions, the cathode electrode usually operates at a potential below 1.0 V vs the reversible hydrogen electrode (V_{RHE}), but during fuel starvation, e.g., start-up and shutdown (SUSD) events, the potential can spike up to 1.5 V_{RHE}.[5,6] While the carbon oxidation reaction (COR) has a thermodynamic onset potential of 0.21 V_{RHE},[7] the effect on the physical structure of the carbon support is very small in the normal potential operating range (<1.0 V_{RHE}) of a PEMFC[8] due to the slow kinetics of the COR. However, when the potential exceeds 1.0 V_{RHE}, the COR proceeds significantly faster, resulting in degradation of the support (carbon corrosion), and the effects of carbon corrosion on the performance of the PEMFC can be significant.[6,9] Perego et al. studied degradation of a PEMFC at two different operation voltage ranges, where during SUSD conditions (cell voltage > 1.0 V), the PEMFC performance declined rapidly after only a few hundred voltage cycles. However, when the PEMFC operated at voltages below 1.0 V, only a minor decrease of the performance was observed after 30,000 cycles,[10] indicating that the higher voltage, where carbon corrosion is more prominent, is detrimental for the fuel cell performance. Furthermore, it has

Received: January 18, 2024
Revised: May 4, 2024
Accepted: May 6, 2024
Published: May 16, 2024

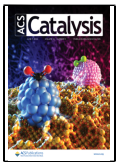

https://doi.org/10.1021/acscatal.4c00417
ACS Catal. 2024, 14, 8494−8504

been shown that carbon corrosion affects the CL by detachment of Pt particles, Pt particle coarsening, and CL compaction.[11] Several studies have found that the presence of Pt accelerates the carbon degradation by catalyzing the COR.[12,13] However, there is a need for a deeper understanding of the mechanism through which carbon corrosion impacts fuel cell performance and the intricate relationship between the mechanical and electrochemical effects of degradation. Furthermore, there is a need to quantify the carbon corrosion rate during operation and its relationship to fuel cell performance losses. Finally, there is a need to identify how CL compaction, growth of Pt particles, or other effects contribute to degradation during SUSD events.[10,14]

Degradation studies of PEMFCs are often performed by a combination of electrochemical characterization, in situ and ex situ microscopy, and/or spectroscopy methods.[15] Electron microscopy imaging, such as identical location (IL) scanning electron microscopy (SEM) and transmission electron microscopy (TEM), can provide valuable insights into the changes that occur in samples over time and have been used to study catalyst degradation for PEMFC applications.[16,17] IL microscopy can be used to identify and distinguish between different types of degradation mechanisms, such as particle growth, particle detachment, and structural deformation. This was done by Vion-Dury et al.,[18] who identified different modes of Pt particle degradation during potential cycling between 0.1 and 0.9 V_{RHE} in 1 M H_2SO_4, and by Zana et al.,[19] who studied the effects of potential cycling in different ranges between 0.4 and 1.5 V_{RHE} in 0.1 M $HClO_4$. In particular, IL microscopy can give insights on the effects of SUSD events, by showing how carbon corrosion affects the morphology of the cathodic catalyst layer (CCL), clarify the significance of, for example, initial defects on further degradation, and distinguish between the effect of carbon corrosion (i.e., COR) and Pt particle growth to help illuminate their respective impact on the performance loss. Our previous studies have shown that it is possible to perform IL-SEM and IL-TEM in a single-cell PEMFC,[8,20] providing a unique and informative perspective on the degradation of the catalyst under realistic operation conditions of the fuel cell.

IL microscopy has traditionally been performed in half-cell configurations with liquid electrolytes at room temperature.[16−19,21] However, these conditions differ substantially from the gaseous environment and elevated temperatures of a PEMFC in operation.[22] The correlation between results achieved in half-cells with a liquid electrolyte, such as rotating disc electrode (RDE) setups, and results from PEMFCs, achieved under real operation conditions, is not evident.[23−25] Lazarids et al. suggest that while it is possible to extrapolate some trends from RDE measurements to PEMFC performance and degradation, it is difficult to obtain absolute values since various factors, like reactants in the gas phase, humidity effects, overpressures, flow rates, and interactions between the membrane and the CL, come into play in PEMFCs but not in RDE.[22] For example, RDE measurements can lead to an overestimation of Pt particle growth and electrochemically active surface area (ECSA) loss or underestimation of effects of carbon support degradation.[26] To better understand the degradation processes that occur under real PEMFC operating conditions, more detailed imaging and analysis of CCL should be performed during degradation under realistic conditions.

In this study, the morphological changes of the CCL during an accelerated stress test (AST) mimicking SUSD events were investigated using IL-TEM and IL-SEM implemented in a 5 cm^2 single-cell fuel cell. IL-SEM was used to observe the degradation of the CCL of the membrane electrode assembly (MEA) on micro- and macroscopic scales, while IL-TEM was used to follow the degradation of the carbon support and Pt nanoparticles on the nanoscopic scale. Electrochemical characterization showed a 2- to 4-fold increase in high-frequency resistance (HFR) and a steep decline in performance from 1.17 A cm^{-2} at the beginning of life (BOL) to ca. 0.24 A cm^{-2} at the end of life (EOL) at 0.7 V, equivalent to a loss of 79% of the initial activity. On the macroscopic scale, cracks developed in the CCL, leading to the exposure of the underlying membrane and a decrease in physical contact within the CCL, which was correlated with the increase in HFR. On the nanoscopic scale, the carbon support was observed to lose volume, forcing Pt particle agglomeration and particle growth. The mean diameter of the Pt particles increased from 3.4 nm at BOL to 5.2 nm at EOL, with several large Pt particles (> 20 nm in diameter) present at EOL, which coincides with a measured 65% loss of ECSA. Furthermore, the carbon support was observed to collapse on weak points, which on a larger scale could lead to compaction of the porous structure.

2. EXPERIMENTAL PART

2.1. Sample Preparation and Work Flow. The MEA consisted of a commercial three-layer catalyst-coated membrane (CCM, IRD Fuel Cells) with a loading of 0.1/0.4 mg_{Pt} cm^{-2} on the anode/cathode and a 5 cm^2 active area, mounted in between two gas diffusion layers (GDLs, GDL 36 BB, SGL SIGRACET), all held together with fiberglass gaskets reinforced with PTFE (Fiberflon).

TEM grids of gold without a carbon film (golden hollow grids, Ted Pella) were used for the IL-TEM studies to avoid the effects of degradation of any carbon film in the grids. Material from the CCL of a fresh CCM was carefully scraped off and mixed with Milli-Q water (18.2 MΩ cm). The catalyst mixture was deposited onto the TEM grids by drop-casting the solution on the TEM grids, after which the grids were let to air-dry. The grids were placed on top of the CCL of a new CCM assembled in a MEA, after which a cathodic GDL was placed on top of the grid, and the full MEA was placed in the fuel cell to press it together. The grids were placed so that they were located under a channel in the flow field.

Before activation of the MEA, and after each AST session, the fuel cell was disassembled, and the cathodic GDL was carefully removed to expose the top side of the CCL and the TEM grid. The CCL was imaged with SEM, while the TEM grid was taken out for imaging with high-resolution (HR) TEM. Details on the disassembly method and SEM and TEM imaging can be found in the Supporting Information (Figure S1) and in previous publications from our group.[8,20] We have previously shown that this type of disassembling and imaging of the MEA does not affect the performance of the fuel cell.[8] After imaging, the TEM grid and GDL were reassembled in the same position on the CCL, and the complete MEA was reinserted into the fuel cell for further testing.

2.2. Fuel Cell Assembly. The experiments were conducted in an in-house-built fuel cell testing system using a single-cell fuel cell (qCF Quick Connect Fixture Unit, BalticFuelCells) with a 5 cm^2 graphite flow field with a serpentine flow pattern. The gases were heated and fully humidified, and their flow rates were controlled by mass flow

https://doi.org/10.1021/acscatal.4c00417
ACS Catal. 2024, 14, 8494−8504

controllers (FG-201CS, Bronkhorst). All gases used were of grade N6.0 purity (Strandmöllen), and the cell pressure was controlled by pressure controllers (P-702CV, Bronkhorst). The MEA was assembled into the fuel cell, which was closed using a pneumatic pressure of 1.5 bar. All electrochemical data was collected using a potentiostat equipped with an 80 A amplifier (HCP-803, BioLogic), and the presented voltages were measured against the anode electrode.

2.3. Electrochemical Protocols. An overview of the electrochemical protocol used to follow fuel cell performance losses and investigate electrode degradation during the AST can be found in Figure 1a. To study the degradation of the

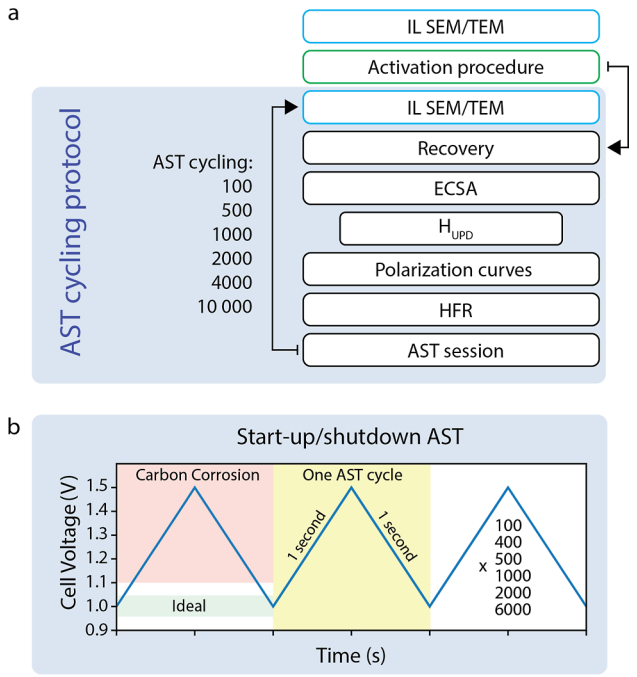

Figure 1. (a) Overview of the electrochemical protocol for the SUSD AST. (b) SUSD AST voltage profile.

carbon support during aggressive conditions such as SUSD events, a triangular wave AST adapted from DOE[27] (hereafter called SUSD AST) was carried out where the cell voltage was cycled between 1.0 and 1.5 V at a scan rate of 500 mV s^{-1}, for a total of 10,000 cycles, with interruption for IL-SEM and IL-TEM imaging after 100, 500, 1000, 2000, 4000, and 10,000 total cycles (Figure 1b). The AST was carried out at 80 °C and 100% relative humidity (RH), with H_2/Ar and with a flow of 100/200 mL min^{-1} at the anode/cathode respectively, at ambient pressure. The MEAs were activated prior to electrochemical testing using 10 chronoamperometry cycles, where each cycle consisted of voltage holds at 0.6 V for 45 min, 0.95 V for 5 min, and finally 0.85 V for 10 min[28] The activation procedure was performed at 60 °C and 100% RH using H_2/air with a gas flow of 140/400 mL min^{-1} on the anode/cathode and a cell pressure of 1.5 barg on both sides.

A recovery procedure was performed after activation and after each AST session to recover reversible losses by holding the cell voltage constant at 0.3 V for 2 h using H_2/air with a flow of 140/400 mL min^{-1} (anode/cathode) at 40 °C and at 100% RH and a cell pressure of 1.5 barg on both sides.[6] After each recovery procedure, cyclic voltammetry (CV) was performed to measure the ECSA by sweeping the cell voltage from 0.07 to 1.0 V at a scan rate of 150 mV s^{-1} at 40 °C and with gas flows of 200/50 mL min^{-1} H_2/Ar at the anode/cathode at ambient pressure. The ECSA was estimated using the hydrogen underpotential deposition (H_{UPD}) region by integrating the charge associated with hydrogen desorption with corrections for double-layer capacitance, assuming a surface charge of 210 μC cm^{-2} for polycrystalline Pt and 100% coverage.[29]

Polarization curves were measured for the MEAs to analyze their activity at BOL and after each AST session, where the cell voltage was kept constant for 2 min at 21 different voltage points from 0.4 to 1.0 V at 80 °C using H_2/air at the anode/cathode with 100% RH and a cell pressure of 1.5 barg on both sides. The current was calculated as an average of the last 60 s. The HFR was measured at BOL and after each AST session by performing electrochemical impedance spectroscopy at 21 different voltages between 0.4 and 1.0 V using a frequency range of 2−100,000 Hz at 80 °C using H_2/air at the anode/cathode with 100% RH and a cell pressure of 1.5 barg on both sides.

2.4. Electron Microscopy. For the IL-SEM imaging, the CCL was imaged after activation and each AST session using SEM (Zeiss Ultra 55 FEG) operating at 5 kV. For the IL-TEM imaging, the TEM grids were imaged with HRTEM (FEI Titan) operating at 300 kV. After imaging, the TEM grids and GDLs were reassembled in the same position on the CCL, and the complete MEA was reinserted into the fuel cell for further testing. Cross sections of a fresh CCM and a CCM at EOL were cut with focused-ion beam (FIB, FEI, Versa3D) and imaged using SEM and HRTEM.

3. RESULTS AND DISCUSSION

The effects of SUSD events on the CCL were studied by using an AST where the cell voltage was cycled between 1.0 and 1.5 V at 500 mV s^{-1}. The polarization curves (Figure 2a) show that the decline in fuel cell performance is minor after the first 100 voltage cycles. However, after 500 cycles, a considerable loss in performance can be seen, with the current at 0.7 V declining from 1.17 A cm^{-2} at BOL to 0.85 A cm^{-2}. The rapid decline of the current continues up to 4000 cycles to ca. 0.24 A cm^{-2} measured at a cell voltage of 0.7 V, equivalent to an 79% loss of the initial performance, after which the performance stabilizes. Significant changes in the HFR can be seen throughout the experiment, from ca. 37 mΩ cm^2 at BOL to about 45−50 mΩ cm^2 after 500 cycles. At EOL, the HFR increased by 2−4 times, to between 80 and 150 mΩ cm^2. By comparison, during voltage cycling below 1.0 V, mimicking normal operation, the degradation of the performance is much less severe, and the change in HFR is negligible.[8]

The CVs (Figure 2b) show that the current from hydrogen adsorption/desorption decreases after each AST session until around 4000 cycles. After 4000 cycles, the CVs seem to stabilize, with only minor changes during the last 6000 cycles. The decrease in H_{UPD} translates to a 65% decrease in ECSA, from 70.9 m^2 g_{Pt}^{-1} at BOL to 24.7 m^2 g_{Pt}^{-1} at EOL. These results are in agreement with previous studies.[10,20]

Figure 2c shows the voltage loss of the polarization curves as a function of normalized ECSA for different current densities. Zihrul et al. demonstrated that if decrease in ECSA was the sole contributor to performance loss during the AST at 80 °C, the voltage loss should be −70 mV dec^{-1} of ECSA loss for all current densities.[30] However, the data in Figure 2c do not follow this trend, especially for higher current densities where

https://doi.org/10.1021/acscatal.4c00417
ACS Catal. 2024, 14, 8494−8504

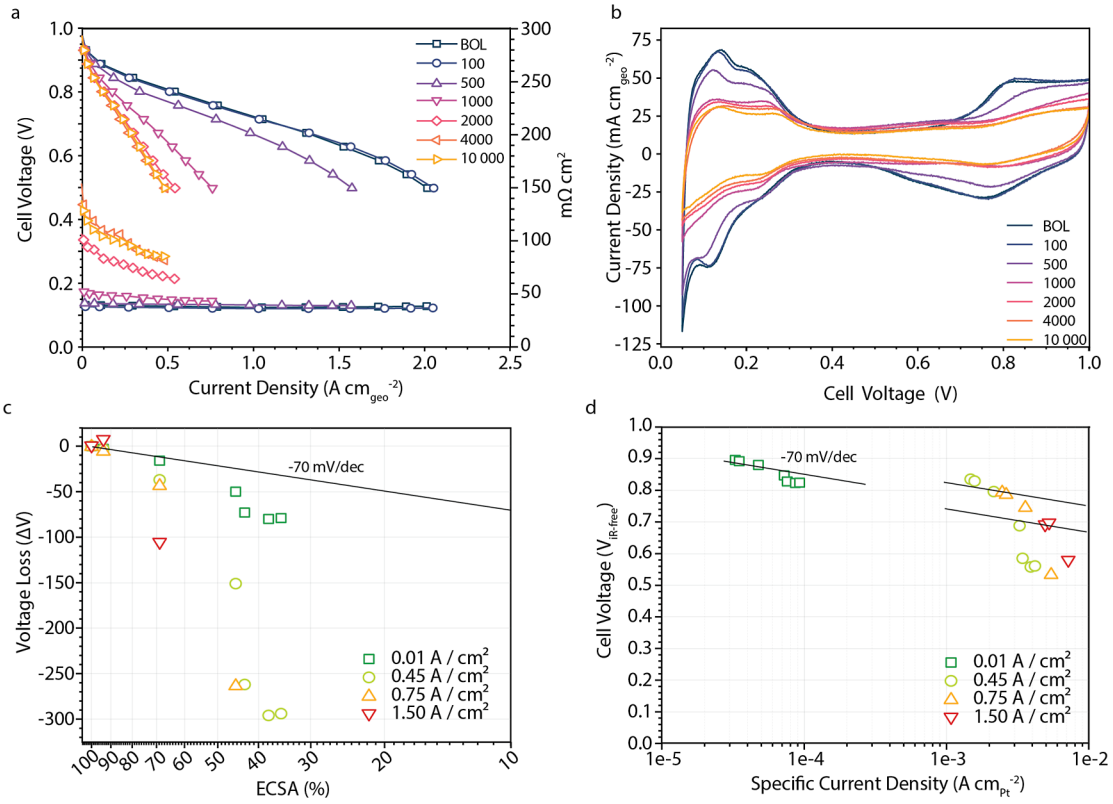

Figure 2. (a) Polarization curves and HFR and (b) CVs recorded after each SUSD AST session. (c) Voltage loss vs normalized ECSA and (d) *iR*-compensated cell voltage vs specific current density for different geometrical current densities. The black lines in (c,d) indicate the predicted voltage loss of −70 mV dec^{-1} based on the decrease of ECSA.

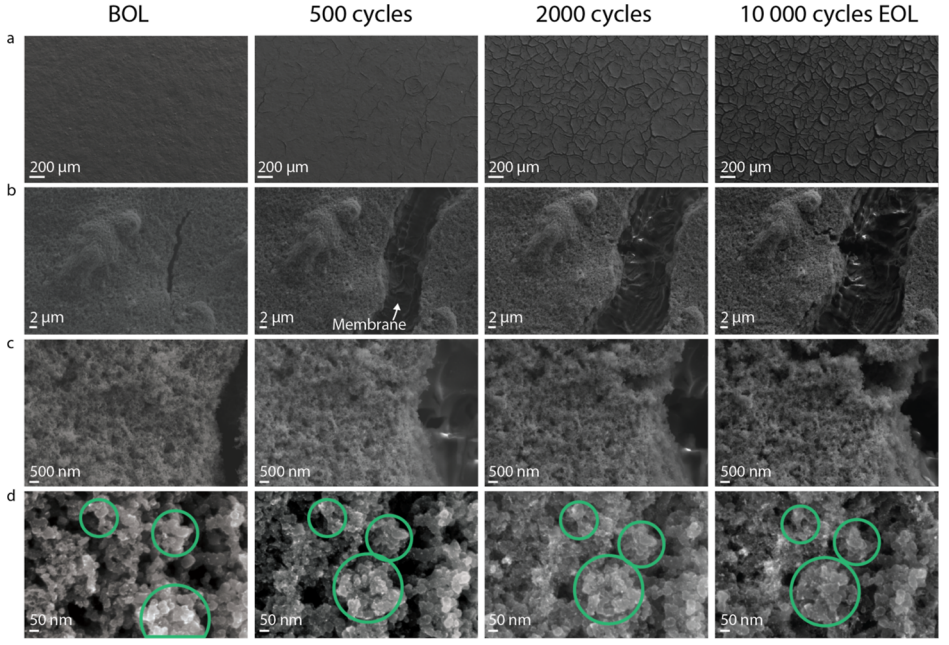

Figure 3. IL-SEM representing the degradation of the CCL during SUSD AST, at BOL, after 500, 2000, and 10,000 cycles at increasing magnification (a−f). Each row is the magnification of the middle area in the row above. The green circles highlight how the position of some carbon aggregates relative to each other changes over the course of the SUSD AST. The white dots visible at higher magnifications (d) are larger Pt particles and Pt particle aggregates. The CL contains many more Pt particles (as visible in the TEM image), but due to their small size, the majority of the Pt particles are not visible in the SEM image under these conditions.

the voltage loss is several times larger than −70 mV dec$^{-1}_{\text{ECSA loss}}$. After 500 SUSD cycles, when the initial ECSA has decreased to approximately 70% of the initial value, only the current density in the kinetic region (0.1 mA cm^{-2}) is still following the −70 mV dec$^{-1}_{\text{ECSA loss}}$ pattern, while higher current densities show significant deviations. Below 50% of the initial ECSA (after ≥

https://doi.org/10.1021/acscatal.4c00417
ACS Catal. 2024, 14, 8494−8504

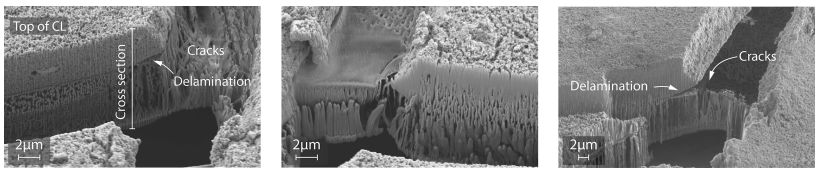

Figure 4. Cross sections of the MEA at EOL, cut via FIB. The left and middle figures are taken from the same cutout but different sides. The cross sections show cracks in the CCL which exposes the membrane in between. The CCL is delaminating from the membrane at the edges of the rifts, and the membrane shows signs of cracks in the exposed part of the membrane.

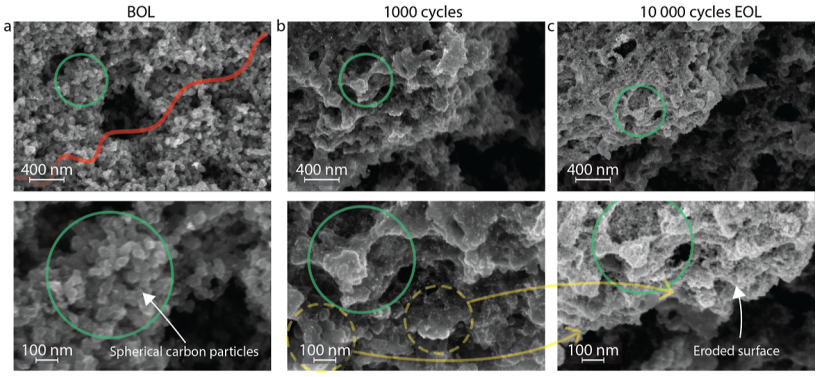

Figure 5. High-magnification IL-SEM imaging from (a) BOL, (b) after 1000 SUSD cycles, and (c) EOL, showing the edge of a crack being formed in the CCL. The red line marks the approximate location at the BOL where a crack is subsequently formed in the CL. The green circles each mark the same feature at different stages of the aging process. The yellow dashed circles highlight aggregations of the carbon support that has detached at EOL.

1000 SUSD cycles), all current densities deviate from the expected behavior of −70 mV $dec^{-1}_{ECSA\ loss}$. Thus, it is clear that ECSA is not the sole nor the main contributor to the performance loss. Figure 2d displays the *iR*-corrected cell voltage as a function of the specific current density. When compensating for resistance losses, the voltage loss at low current densities (0.01 A cm^{-2}) follows a trend of −70 mV $dec^{-1}_{ECSA\ loss}$ more closely. Thus, the change in resistance is a significant contributor to voltage loss in the kinetic region. At higher current densities (0.45 and 0.75 A cm^{-2}) where the trend was lost already at 70% ECSA after 500 SUSD cycles before *iR* correction, the trend is now lost after 1000 cycles. This indicates that while voltage losses initially are due to increased ohmic resistance, as the degradation progresses, mass transport limitations and other factors become significant contributors. Furthermore, at even higher current densities (1.5 A cm^{-2}), the data deviates from the −70 mV dec^{-1} trend almost immediately, even after *iR* correction. This indicates that mass transport limitations and other factors contribute significantly to the voltage loss at these higher current densities.

IL microscopy was performed to give insight into the cause of the ECSA loss and a decrease in the activity of the MEA during the SUSD AST. IL-SEM imaging from BOL, and after 500, 2000, and 10,000 cycles (Figure 3), shows the macroscopic scale morphological changes to the CCL. The images in Figure 3 were taken from near the outlet of the flow field. The full set of IL-SEM images from the MEA at BOL, and after 100, 500, 1000, 2000, 4000, and 10,000 cycles, can be found in the Supporting Information (Figure S2). At BOL, the surface is mainly flat and homogeneous, with some minor defects from production and prehandling in the form of cracks and protruding surface structures. After SUSD cycling, the pre-existing cracks grow and widen, and many more cracks form, exposing the proton-exchange membrane underneath. While the initial defects grow during the aging process, they only make up a fraction of the cracks at EOL, and they are not significantly larger or more severe than other cracks. This indicates that minor but visible defects from the production process are not the origin of the majority of cracks seen during later stages of degradation. Some carbon particles that appear to have detached from the main structure can be seen on the membrane exposed in the cracks, where they have no electrical contact and can thus not take part in electrochemical reactions. Higher magnification images of the exposed membrane and detached carbon aggregates can be seen in Figure S6a−b. The cracks continue to grow with further SUSD cycling, and eventually, the cracks cover the whole surface, separating the CCL into isolated islands. Furthermore, the edges of these islands show signs of delaminating from the membrane, as more clearly illustrated in FIB cross sections (Figure 4). The reduced contact between the CCL and the membrane due to delamination and separation of the CCL to isolated islands can help explain the considerable increase in resistance seen in Figure 2. For a MEA subjected to 10,000 SUSD cycles without intermediate disassembling/SEM analysis/assembling until EOL characterization showed similar features of crack formation and primary carbon sphere corrosion (Figure S3). However, no signs of crack formation or carbon sphere erosion were found after only MEA assembling/disassembling without voltage cycling or after IL-SEM measurements performed on the same type of MEAs subjected to lower voltage ranges (<1.0 V)[8] (Figures S4 and S5). Thus, the formation of cracks must be driven by the voltage range and not by the cell disassembly or SEM imaging. The formation of cracks likely stems from the volume loss of the CL due to conversion of carbon to CO_2. Volume loss can cause strain within the CL, which in turn can lead to the formation and propagation of cracks. Moreover, weak points between carbon aggregates are prone to breaking due to carbon corrosion, forming initiation sites for crack

https://doi.org/10.1021/acscatal.4c00417
ACS Catal. 2024, 14, 8494−8504

formation. Furthermore, the SEM images show rifts being formed in the membrane that is exposed through the cracks (Figure 3b,c), which can also be seen in the cross section (Figure 4). If these rifts extend through the entire membrane to the anodic CL creating pinholes, it would lead to increased rate of hydrogen crossover, negatively impacting the efficiency of the fuel cell and increase the rate of degradation, and ultimately lead to MEA failure.[31,32]

Further insights into the impact of carbon corrosion can be gained from the high-magnification IL-SEM images. Figure 5 shows a high-magnification view of the formation of a crevice from BOL, after 1000 SUSD cycles, and EOL. The full set of images can be found in the Supporting Information (Figure S2d,e). Green circles mark the same location, and the red zigzag line marks where the crevice is later formed. At BOL, the carbon support consists of aggregated spherical primary carbon particles ranging from 30 to 50 nm forming a porous structure. After SUSD cycling, these primary carbon particles erode, losing their spherical shape, and chunks of carbon (yellow circles) detach, probably due to weakening and corrosion of the anchor points. The loss of structure of the carbon support indicates a change in the porous structure, which is known to occur during carbon corroding conditions and has been correlated with an increase in mass-transfer resistance and water accumulation.[33] Moreover, the carbon support fragments that have detached likely do not have good contact with the rest of the CCL where they have reattached, such as the CL residue seen on the membrane in the cracks (Figure S6). It is likely that the Pt particles still present on these carbon support fragments are not accessible electrochemically and thus are not measured in the ECSA, contributing to ECSA loss.

Figure 6 shows a schematic illustration of the degradation of the CCL observed by IL-SEM. At BOL, the CCL is fully covering the membrane. During SUSD cycling, crevices are formed in the CL, exposing the membrane underneath. Small rifts start to form in the exposed membrane. With further SUSD cycling, the rifts in the membrane deepen and the crevices in the CCL widen. Eventually, the edges of the CCL islands start to delaminate from the membrane, exposing them even more.

In Figure 7, IL-TEM images show the degradation of both the carbon support and the Pt particles on a nanoscopic scale from BOL and after 500, 2000, and 10,000 SUSD cycles. The full set of IL-TEM images from BOL, 100, 500, 1000, 2000, 4000, and 10,000 cycles can be found in the Supporting Information (Figure S7). At BOL, Pt particles, measuring 2−4 nm in diameter, are evenly distributed on the carbon support. After cycling, the Pt particles merge and grow in size, and at EOL, many particles > 20 nm in diameter are present all over the sample. The images from BOL show spherical primary particles of the carbon support, forming porous aggregates. After SUSD cycling, the carbon support can be seen to gradually lose volume, as the carbon is being oxidized to CO_2. TEM imaging using an acceleration voltage of 300 kV has in previous studies been found to not affect the carbon support;[20] thus, we conclude that the observed degradation of the carbon support is a result of the high potential cycling and not caused by the imaging method. After a few hundred voltage cycles, some weak points of the carbon support have broken and, as a consequence, fragments of the carbon support structure have detached (Figure 7a). This can be compared to the cracks that can be seen to form early in the degradation process in the IL-

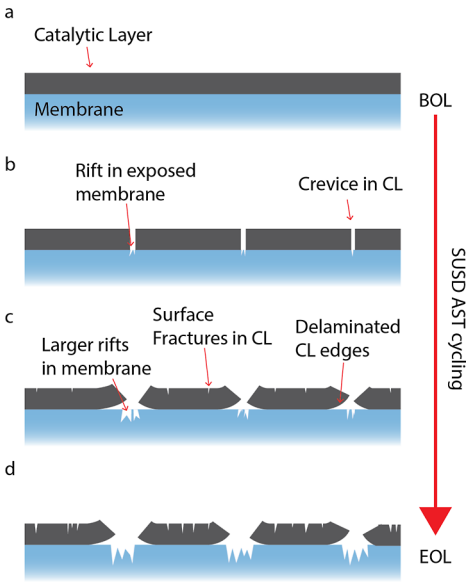

Figure 6. Schematic illustration of the degradation of the CCL and membrane based on the SEM images (Figures 3−5). (a) At BOL, the CCL fully covers the membrane. (b) After a few hundred SUSD cycles, crevices appear in the CCL along with small rifts in the exposed membrane. (c) Eventually, the edges of the CCL start to delaminate and disconnect from the membrane, and more fractures are created on the surface of the CL. Moreover, the rift in the membrane deepens. (d) Further cycling leads to more severe degradation.

SEM images (Figure 3), where weak points in the carbon structure break, creating cracks on a larger scale through the CCL that later propagate. Detached fragments of the CCL can also be seen in the IL-SEM images as clumps of carbon on the exposed membrane. The remaining carbon support continuously loses volume during the AST (Figures 7b,c and S7), which brings the Pt particles into closer proximity to each other. Rasouli et al. also reported movement of Pt particles on the carbon support during SUSD conditions and attribute this to carbon corrosion underneath the Pt particle, likely catalyzed by the Pt particle itself.[34] Between 4000 and 10,000 cycles, the carbon support tends to collapse on itself, changing the porous structure. On a larger scale, this effect can lead to a compaction of the CCL layer, thereby limit mass transport and reduce activity at higher current densities.[33,35] The degree of carbon support degradation observed in Figure 7 is more severe than what has been reported by Schonvogel et al., who showed IL-TEM imaging of degradation of Pt supported on different types of carbon support during cycling up to 1.4 V vs the standard hydrogen electrode in a liquid electrolyte,[21] highlighting the importance of performing degradation studies in realistic conditions for better understanding of the importance of different degradation mechanisms.

Figure 8a,b shows high-magnification images of two different areas of the CL, one with relatively low density of Pt particles and one area with higher density of Pt particles, respectively. Pt is known to catalyze the COR,[12,13,36] which would indicate that areas with higher Pt densities could locally have a higher rate of carbon corrosion. This could be the case seen here, where the carbon support with high Pt density has shrunk considerably at EOL compared to the area with lower Pt density. However, areas with a higher Pt density are also more prone to Pt growth by Ostwald ripening and particle

https://doi.org/10.1021/acscatal.4c00417
ACS Catal. 2024, 14, 8494−8504

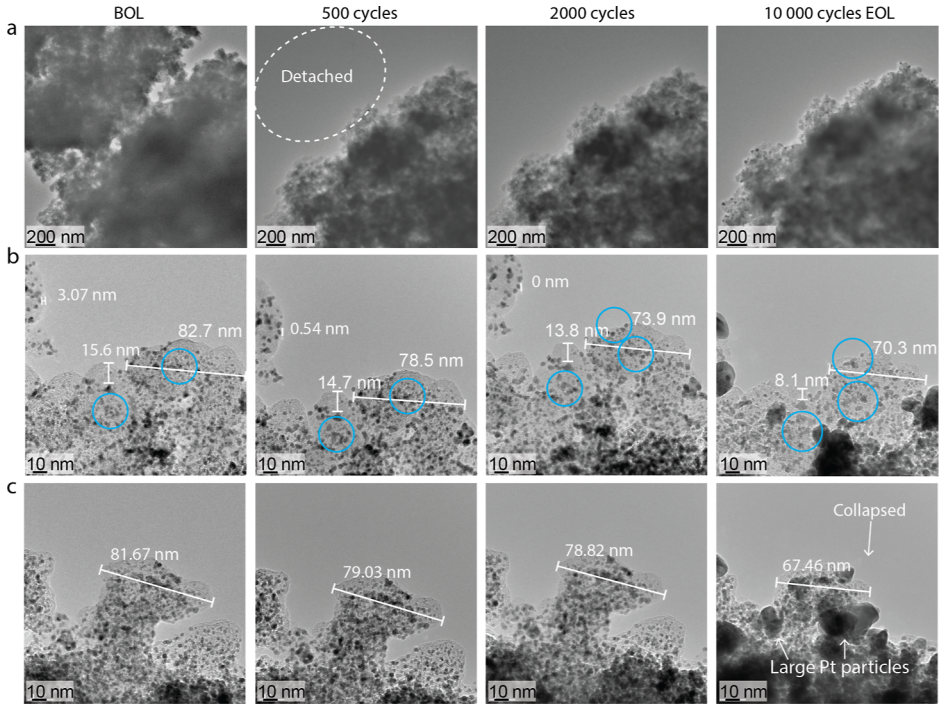

Figure 7. IL-TEM images from BOL and after 500, 2000, and 10,000 total SUSD cycles. (a) Overview showing a large piece of CL detaching at a weak connection point and (b,c) high-magnification views of representative areas.

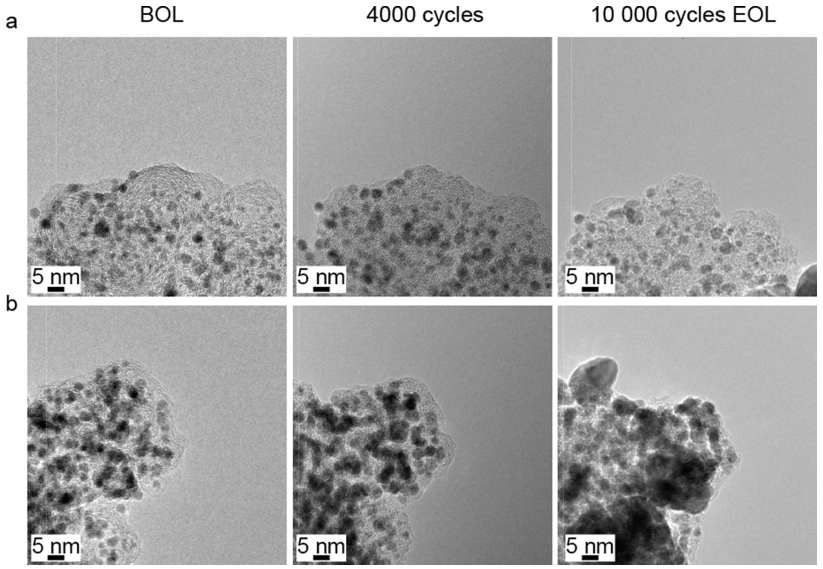

Figure 8. High-magnification IL-TEM images on the edge to focus on the surface, at (left) BOL, (middle) after 4000, and (right) after 10,000 SUSD cycles. (a) Representative average region on the CL. (b) Region with high density of Pt particles.

coalescence, which might also explain the changes seen in the area with a high Pt density.

To create Pt particle size histograms, the diameter of 500 Pt particles was measured after each AST session from the same locations in the TEM images (Figure S7). The mean Pt particle size increased by 53% during the AST, from 3.4 nm at BOL to 5.2 nm at EOL (Figure 9b). This is in good agreement with the previously reported data. For example, Qi et al. measured Pt growth during a similar SUSD AST using X-ray diffraction (XRD) and reported a growth of the Pt particles from 3.4 nm at BOL to 5.4 nm after 10,000 SUSD cycles.[14] This increase is larger than seen during normal operation conditions below 1.0 V,[20] likely caused by the shrinking of the carbon support forcing the Pt particles closer, which promotes agglomeration and coalescence. Similar effects were observed by Hu et al.,[36] who studied carbon corrosion using in situ liquid TEM. The observed shrinking of the carbon support result in coalescence of the supported Pt particles, leading to Pt growth. Other effects, such as Ostwald ripening, may also influence Pt particle growth, although the overall impact is hard to quantify.

Furthermore, in the TEM images (Figure 7) at EOL, many large Pt particles, > 15 nm, can be seen all over the carbon support. Such large particles are not seen at BOL, nor after

https://doi.org/10.1021/acscatal.4c00417
ACS Catal. 2024, 14, 8494−8504

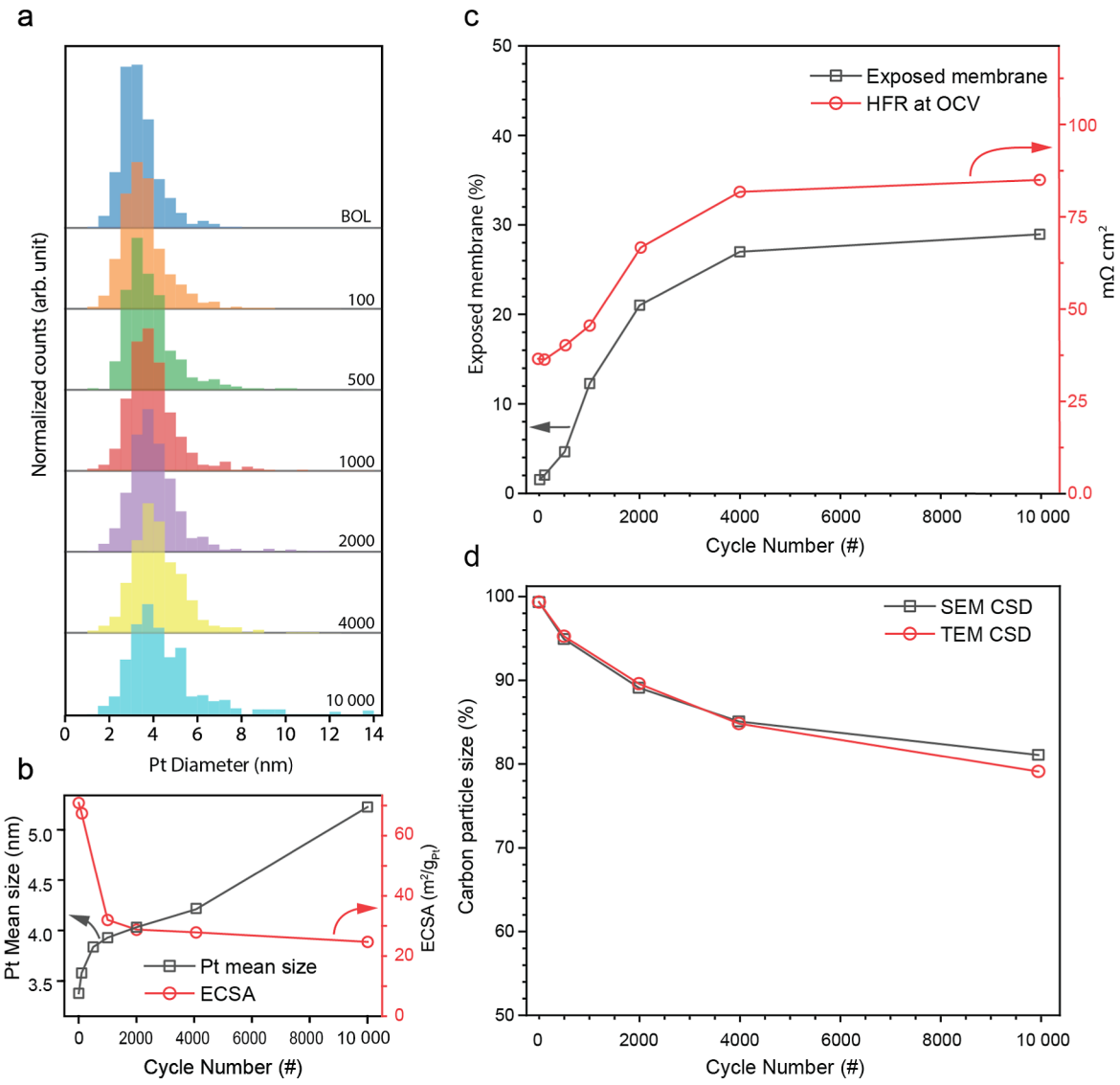

Figure 9. (a) Size distributions of Pt particles calculated from the same location of the IL-TEM images from BOL and after 100, 500, 1000, 2000, 4000, and 10,000 total SUSD cycles. The histograms are limited to below 14 nm; however, particles up to 30 nm in diameter were seen on the sample. (b) Mean Pt diameter (black squares) and ECSA (red circles) after each AST session. The full set of particles was used to calculate the Pt particle mean size. (c) Percent of surface with exposed membrane, extracted from the IL-SEM images of the CCL (black squares), and HFR at open-circuit voltage (from data in Figure 2, red circles). (d) Change in average diameter of the primary carbon support particles measured from IL-SEM images (gray squares) and IL-TEM images (red circles). The carbon particle size is measured from the same particles at each point in time.

voltage cycling at lower potential ranges,[20] showing that it is the SUSD cycling which causes their formation. Similar large particles can also be seen in the TEM images of FIB cross sections from a MEA at EOL (Figure S8), showing that similar effects are present throughout the MEA, and not only locally on the TEM grids.

The surface coverage of cracks, i.e., the amount of the surface with cracks or exposed membrane, was calculated from IL-SEM images such as those in Figures 3 and S2 and is shown in Figure 9c. At BOL, the amount of cracks and exposed membrane is negligible, corresponding to the homogeneous CCL surface seen in Figure 3a. After 100 SUSD cycles, cracks have started to form in the CL, which exposes the underlying membrane. As more cracks are formed and grow with further SUSD cycling, the amount of exposed membrane increases, and after 2000 cycles, 21% of the surface is covered by cracks. After 4000 cycles, the crack growth decelerated, causing a plateau in the expansion of the exposed membrane. At EOL, around 27% of the CCL is composed of cracks or exposed membrane.

The amount of exposed membrane on the surface of the CCL is plotted as a function of the number of SUSD cycles and is shown in Figure 9c. In Figure 9c, we have also plotted the changes in HFR resistance (from Figure 2), and as can be seen, the trends for increased amount of exposed membrane and increase in HFR are very similar. As the carbon particle size and the coverage decrease, the cell resistance increases and the performance decreases. As the decrease of the carbon support and CCL coverage level out after 4000 cycles, so does the resistance, even though the Pt particles continue to grow up to 10,000 cycles. Likely, it is the loss of physical contact between the CL, membrane, and GDL that is the main effect responsible for the increase of cell resistance, which together with mass transport limitations from compaction of the porous

https://doi.org/10.1021/acscatal.4c00417
ACS Catal. 2024, 14, 8494−8504

structure leads to the severe performance loss, while Pt particle growth is of less importance. Furthermore, loss of an ionomer due to oxidation could also reduce the electrical contact within the CCL and lead to a resistance increase.

Figure 9d shows the decrease in the size of the primary carbon spheres, measured from the IL-SEM and IL-TEM images (see the Supporting Information for details). This decrease in size is measured from the same particles after each AST session. Measured from IL-SEM, the carbon spheres shrink to 80% of their initial width after 10,000 cycles. The IL-TEM images yield comparable findings, where the carbon structures, on average, shrink to approximately 79% of their initial width. This decrease in size stabilizes between 4000 and 10,000 cycles in both cases. While some of the observed changes in appearance of the carbon particles could be due to 3-dimensional rotation of the carbon support, it is unlikely that such a movement would give a consistent decrease in size over the course of the AST at all observed locations. This congruence between IL-SEM and IL-TEM measurements is a good indication that the degradation of the sample on the TEM grid is representative of the degradation of the CL and shows that even if IL-TEM is a more localized technique giving data from a smaller part of the sample than IL-SEM, IL-TEM can still be used to give good quantifiable data and to describe the interface at the nanometer level. However, it should be noted that the IL-SEM and the IL-TEM techniques presented here only show degradation at the interface between the CCL and the GDL, as the SEM imaging only shows the top view of the CCL, and the TEM grids are placed on top of the CCL closest to the GDL. Thus, neither of these two techniques show degradation of the CCL closer to the membrane, where the CCL degradation is known to differ, by e.g., tending to form a Pt depletion zone near the membrane/cathode interface.[35]

4. CONCLUSIONS

The effects of voltage cycling during an AST, mimicking SUSD conditions, on the CCL in a PEMFC was studied using IL-SEM and IL-TEM, together with electrochemical characterization. The voltage cycling results in strong performance losses already after 500 cycles and a significant increase in cell resistance. Loss of carbon volume due to CO_2 formation causes the CCL to shrink, leading to crack formation in the CCL, likely due to internal strain. These cracks expose the underlying membrane and propagate, eventually spanning the whole CCL surface and forming isolated islands of the CCL. The edges of these CCL islands tend to delaminate from the membrane, decreasing physical contact. This decrease in contact coincides to a 2- to 4-fold increase in HFR. Loss of carbon volume forces Pt particles closer, promoting Pt growth, which contributes to loss of ECSA. Resistance increase and mass transport limitations were found to have more influence than the ECSA decrease on the performance loss of the fuel cell.

The performance declines steeply up to 4000 cycles, from 1.17 A cm^{-2} at BOL to ca. 0.24 A cm^{-2} at 0.7 V, after which it stabilizes, with minimal further losses during the last 6000 cycles. The performance loss and resistance increase coincide with a decrease in CCL coverage due to the formation and growth of cracks, which all level out after 4000 cycles. Similar trends in carbon shrinkage can be seen in both the IL-SEM and the IL-TEM images, where the majority of the carbon volume loss occurs during the first 4000 cycles, where the carbon spheres shrink by about 15% from BOL. At EOL, between 19 and 21% of the initial carbon sphere diameter is lost. While defects such as rifts present on the CCL at BOL in the CCL grow during the AST, their overall effect is small since a large amount of rifts form in the initially defect-free CCL already after 100 cycles, and the rifts formed from initial defects do not seem to grow larger than rifts formed later during the AST, indicating that defects from production or handling are not detrimental.

When compared to previous studies performed using lower voltage ranges (0.6−1.0 V),[8,20] the degradation of the CCL and the concurrent decrease in fuel cell performance are much more severe, and the Pt particles grow more during the SUSD conditions presented here, by 53% from 3.4 to 5.2 nm compared to 27% from 3.3 to 4.2 nm at lower voltage ranges (0.6−1.0 V).[20] SUSD conditions cause several effects that negatively affect the performance and lifetime of the fuel cell and should be avoided with mitigating strategies and well-designed fuel cell systems.

■ ASSOCIATED CONTENT

Supporting Information

The Supporting Information is available free of charge at https://pubs.acs.org/doi/10.1021/acscatal.4c00417.

Details on fuel cell disassembly/assembly and SEM imaging; SEM and TEM images from BOL, and after 100, 500, 1000, 2000, 4000, and 10,000 SUSD cycles; SEM images from EOL with and without IL-SEM; IL-SEM images of effects of disassembly/assembly; SEM images from BOL, and after 1000, 5000, and 15,000 voltage cycles between 0.6 V and OCV; SEM images of the catalyst material on the exposed membrane; TEM images of cross sections of a fresh MEA, and a MEA after 10,000 SUSD cycles, cut with FIB; and details on measurements of carbon size (PDF)

■ AUTHOR INFORMATION

Corresponding Authors

Linnéa Strandberg − *Department of Physics and Competence Centre for Catalysis, Chalmers University of Technology, Göteborg SE-412 96, Sweden;* orcid.org/0000-0002-0499-4132; Email: linnea.strandberg@chalmers.se

Björn Wickman − *Department of Physics and Competence Centre for Catalysis, Chalmers University of Technology, Göteborg SE-412 96, Sweden;* orcid.org/0000-0001-7119-9529; Email: bjorn.wickman@chalmers.se

Authors

Victor Shokhen − *Department of Physics and Competence Centre for Catalysis, Chalmers University of Technology, Göteborg SE-412 96, Sweden;* orcid.org/0000-0002-9990-2041

Magnus Skoglundh − *Department of Chemistry and Chemical Engineering and Competence Centre for Catalysis, Chalmers University of Technology, Göteborg SE-412 96, Sweden*

Complete contact information is available at: https://pubs.acs.org/10.1021/acscatal.4c00417

Author Contributions

‖L.S. and V.S. contributed equally to this paper.

Notes

The authors declare no competing financial interest.

https://doi.org/10.1021/acscatal.4c00417
ACS Catal. 2024, 14, 8494−8504

■ ACKNOWLEDGMENTS

This project was financially supported by the Swedish Foundation for Strategic Research (project no. ARC19-0026) and the Swedish Research Council (project no. 2018-03927) and performed within the Competence Centre for Catalysis, which is hosted by the Chalmers University of Technology and financially supported by the Swedish Energy Agency (project no. 52689-1) and the member companies Johnson Matthey, Perstorp, PowerCell, Preem, Scania CV, Umicore and Volvo Group. Physical characterization was performed at Chalmers Materials Analysis Laboratory (CMAL).

■ REFERENCES

(1) Cano, Z. P.; Banham, D.; Ye, S.; Hintennach, A.; Lu, J.; Fowler, M.; Chen, Z. Batteries and fuel cells for emerging electric vehicle markets. *Nat. Energy* **2018**, *3*, 279−289.
(2) Eberle, U.; Müller, B.; Von Helmolt, R. Fuel cell electric vehicles and hydrogen infrastructure: status 2012. *Energy Environ. Sci.* **2012**, *5*, 8780−8798.
(3) Cullen, D. A.; Neyerlin, K. C.; Ahluwalia, R. K.; Mukundan, R.; More, K. L.; Borup, R. L.; Weber, A. Z.; Myers, D. J.; Kusoglu, A. New roads and challenges for fuel cells in heavy-duty transportation. *Nat. Energy* **2021**, *6*, 462−474.
(4) Yoshida, T.; Kojima, K. Toyota MIRAI fuel cell vehicle and progress toward a future hydrogen society. *Electrochem. Soc. Interface* **2015**, *24*, 45−49.
(5) Reiser, C. A.; Bregoli, L.; Patterson, T. W.; Yi, J. S.; Yang, J. D.; Perry, M. L.; Jarvi, T. D. A reverse-current decay mechanism for fuel cells. *Electrochem. Solid-State Lett.* **2005**, *8*, A273.
(6) Harzer, G. S.; Schwämmlein, J. N.; Damjanović, A. M.; Ghosh, S.; Gasteiger, H. A. Cathode loading impact on voltage cycling induced PEMFC degradation: a voltage loss analysis. *J. Electrochem. Soc.* **2018**, *165*, F3118−F3131.
(7) Macauley, N.; Papadias, D. D.; Fairweather, J.; Spernjak, D.; Langlois, D.; Ahluwalia, R.; More, K. L.; Mukundan, R.; Borup, R. L. Carbon corrosion in PEM fuel cells and the development of accelerated stress tests. *J. Electrochem. Soc.* **2018**, *165*, F3148−F3160.
(8) Shokhen, V.; Strandberg, L.; Skoglundh, M.; Wickman, B. Impact of Accelerated Stress Tests on the Cathodic Catalytic Layer in a Proton Exchange Membrane (PEM) Fuel Cell Studied by Identical Location Scanning Electron Microscopy. *ACS Appl. Energy Mater.* **2022**, *5*, 11200−11212.
(9) Schwämmlein, J. N.; Rheinländer, P. J.; Chen, Y.; Freyer, K.; Gasteiger, H. Anode aging during PEMFC start-up and shut-down: H2-air fronts vs voltage cycles. *J. Electrochem. Soc.* **2018**, *165*, F1312−F1322.
(10) Perego, A.; Avid, A.; Mamania, D. N.; Chen, Y.; Atanassov, P.; Yildirim, H.; Odgaard, M.; Zenyuk, I. V. Investigation of cathode catalyst layer interfaces evolution during accelerated stress tests for polymer electrolyte fuel cells. *Appl. Catal., B* **2022**, *301*, 120810.
(11) Schulenburg, H.; Schwanitz, B.; Linse, N.; Scherer, G. G.; Wokaun, A.; Krbanjevic, J.; Grothausmann, R.; Manke, I. 3D imaging of catalyst support corrosion in polymer electrolyte fuel cells. *J. Phys. Chem. C* **2011**, *115*, 14236−14243.
(12) Roen, L.; Paik, C.; Jarvi, T. Electrocatalytic corrosion of carbon support in PEMFC cathodes. *Electrochem. Solid-State Lett.* **2004**, *7*, A19.
(13) Wickman, B.; Grönbeck, H.; Hanarp, P.; Kasemo, B. Corrosion induced degradation of Pt/C model electrodes measured with electrochemical quartz crystal microbalance. *J. Electrochem. Soc.* **2010**, *157*, B592.
(14) Qi, Y.; Huang, Y.; Gao, Z.; Chen, C. H.; Perego, A.; Yildirim, H.; Odgaard, M.; Asset, T.; Atanassov, P.; Zenyuk, I. V. Insight into carbon corrosion of different carbon supports for Pt-based electrocatalysts using accelerated stress tests in polymer electrolyte fuel cells. *J. Power Sources* **2022**, *551*, 232209.
(15) Chattot, R.; Roiron, C.; Kumar, K.; Martin, V.; Campos Roldan, C. A.; Mirolo, M.; Martens, I.; Castanheira, L.; Viola, A.; Bacabe, R.; et al. Break-In Bad: On the Conditioning of Fuel Cell Nanoalloy Catalysts. *ACS Catal.* **2022**, *12*, 15675−15685.
(16) Zadick, A.; Dubau, L.; Demirci, U. B.; Chatenet, M. Effects of Pd nanoparticle size and solution reducer strength on Pd/C electrocatalyst stability in alkaline electrolyte. *J. Electrochem. Soc.* **2016**, *163*, F781−F787.
(17) Lafforgue, C.; Maillard, F.; Martin, V.; Dubau, L.; Chatenet, M. Degradation of carbon-supported platinum-group-metal electrocatalysts in alkaline media studied by in situ Fourier transform infrared spectroscopy and identical-location transmission electron microscopy. *ACS Catal.* **2019**, *9*, 5613−5622.
(18) Vion-Dury, B.; Chatenet, M.; Guétaz, L.; Maillard, F. Determination of aging markers and their use as a tool to characterize Pt/C nanoparticles degradation mechanism in model PEMFC cathode environment. *ECS Trans.* **2011**, *41*, 697−708.
(19) Zana, A.; Speder, J.; Roefzaad, M.; Altmann, L.; Bäumer, M.; Arenz, M. Probing degradation by IL-TEM: the influence of stress test conditions on the degradation mechanism. *J. Electrochem. Soc.* **2013**, *160*, F608−F615.
(20) Shokhen, V.; Strandberg, L.; Skoglundh, M.; Wickman, B. Fuel cell electrode degradation followed by identical location transmission electron microscopy. *J. Mater. Chem. A* **2023**, *11*, 21029−21035.
(21) Schonvogel, D.; Hülstede, J.; Wagner, P.; Kruusenberg, I.; Tammeveski, K.; Dyck, A.; Agert, C.; Wark, M. Stability of Pt nanoparticles on alternative carbon supports for oxygen reduction reaction. *J. Electrochem. Soc.* **2017**, *164*, F995−F1004.
(22) Lazaridis, T.; Stühmeier, B. M.; Gasteiger, H. A.; El-Sayed, H. A. Capabilities and limitations of rotating disk electrodes versus membrane electrode assemblies in the investigation of electrocatalysts. *Nat. Catal.* **2022**, *5*, 363−373.
(23) Alinejad, S.; Inaba, M.; Schröder, J.; Du, J.; Quinson, J.; Zana, A.; Arenz, M. Testing fuel cell catalysts under more realistic reaction conditions: accelerated stress tests in a gas diffusion electrode setup. *J. Phys.: Energy* **2020**, *2*, 024003.
(24) Lafforgue, C.; Chatenet, M.; Dubau, L.; Dekel, D. R. Accelerated Stress Test of Pt/C Nanoparticles in an Interface with an Anion-Exchange Membrane- An Identical-Location Transmission Electron Microscopy Study. *ACS Catal.* **2018**, *8*, 1278−1286.
(25) Fan, J.; Chen, M.; Zhao, Z.; Zhang, Z.; Ye, S.; Xu, S.; Wang, H.; Li, H. Bridging the gap between highly active oxygen reduction reaction catalysts and effective catalyst layers for proton exchange membrane fuel cells. *Nat. Energy* **2021**, *6*, 475−486.
(26) Sharma, R.; Andersen, S. M. Quantification on degradation mechanisms of polymer electrolyte membrane fuel cell catalyst layers during an accelerated stress test. *ACS Catal.* **2018**, *8*, 3424−3434.
(27) Team, F. C. T. *Fuel Cell Technical Team Roadmap*, 2017.
(28) Marić, R.; Gebauer, C.; Nesselberger, M.; Hasché, F.; Strasser, P. Towards a Harmonized Accelerated Stress Test Protocol for Fuel Starvation Induced Cell Reversal Events in PEM Fuel Cells: The Effect of Pulse Duration. *J. Electrochem. Soc.* **2020**, *167*, 124520.
(29) Brummer, S. The use of large anodic galvanostatic transients to evaluate the maximum adsorption on platinum from formic acid solutions. *J. Phys. Chem.* **1965**, *69*, 562−571.
(30) Zihrul, P.; Hartung, I.; Kirsch, S.; Huebner, G.; Hasché, F.; Gasteiger, H. A. Voltage cycling induced losses in electrochemically active surface area and in H2/air-performance of PEM fuel cells. *J. Electrochem. Soc.* **2016**, *163*, F492−F498.
(31) Tang, Q.; Li, B.; Yang, D.; Ming, P.; Zhang, C.; Wang, Y. Review of hydrogen crossover through the polymer electrolyte membrane. *Int. J. Hydrogen Energy* **2021**, *46*, 22040−22061.
(32) Huang, B. T.; Chatillon, Y.; Bonnet, C.; Lapicque, F.; Leclerc, S.; Hinaje, M.; Raël, S. Experimental investigation of pinhole effect on MEA/cell aging in PEMFC. *Int. J. Hydrogen Energy* **2013**, *38*, 543−550.
(33) Chen, H.; Zhao, X.; Zhang, T.; Pei, P. The reactant starvation of the proton exchange membrane fuel cells for vehicular applications: A review. *Energy Convers. Manage.* **2019**, *182*, 282−298.

https://doi.org/10.1021/acscatal.4c00417
ACS Catal. 2024, 14, 8494−8504

(34) Rasouli, S.; Myers, D.; Higashida, K.; Nakashima, N.; Crozier, P.; Ferreira, P. Electrochemical Evolution of Fuel Cell Platinum Nanocatalysts on Carbon Nanotubes at the Atomic Scale. *ACS Appl. Energy Mater.* **2023**, *6*, 11861−11873.
(35) Li, J.; He, P.; Wang, K.; Davis, M.; Ye, S. Characterization of catalyst layer structural changes in PEMFC as a function of durability testing. *ECS Trans.* **2006**, *3*, 743−751.
(36) Hu, H.; Liu, Y.; Shi, F.; Tao, P.; Song, C.; Shang, W.; Ke, X.; Deng, T.; Zeng, X.; Wu, J. Corrosion Dynamics of Carbon-Supported Platinum Electrocatalysts with Metal−Carbon Interactions Revealed by In Situ Liquid Transmission Electron Microscopy. *Nano Lett.* **2024**, *24*, 2157−2164.

https://doi.org/10.1021/acscatal.4c00417
ACS Catal. 2024, 14, 8494−8504